Bifurcation Analysis of Parallel-Connected Voltage-Source Inverters With Constant Power Loads

Eduardo Lenz, Daniel J. Pagano, *Member, IEEE*, and Josep Pou, *Fellow, IEEE*

Abstract—This paper focuses on the stability analysis of a small ac microgrid with two inductive droop inverters driving several identical three-phase controlled rectifiers, which are modeled as time-invariant nonlinear dynamical constant power loads. A reduced model is adopted for this microgrid, which only considers the inverter output characteristics, the rectifier input properties, and the transmission line dynamics. Based on this reduced model, the microgrid stability is analyzed for different values of load power using a bifurcation analysis approach.

Index Terms—Droop control, load sharing, dynamic constant power load, virtual impedance, bifurcation analysis.

I. Introduction

IN MICROGRIDS, an important issue is the parallel operation of voltage source converters, and droop control [1], [2] is the standard technique for inverters working in parallel. Whenever droop control is used, the inverter output voltage and frequency become dependent on its output active and reactive powers, which makes the system dynamic more intricate. Also, the type of droop control must match the dc-ac power converter output impedance, and it may be necessary to change the inverter output impedance, which can be performed through the virtual impedance control loop [3].

The main purpose of this paper is to study the dynamics of a small islanded ac microgrid composed by two inverters operating in parallel with droop control and virtual impedance, and four identical time-invariant nonlinear loads. When a microgrid is connected to the main grid, which is usually assumed to be an infinite bus, it decouples all the elements in the microgrid. But without the main grid, the common bus may have a low electrical inertia, which increases the interaction between sources and loads. A study of the microgrid dynamics by means of numerical simulations for the whole system

is helpful, but it can be time consuming and, sometimes, a tedious method. An alternative to this problem is to develop reduced models for the system that can extract just the essence of the microgrid dynamical behavior by overlooking the power converter internal dynamics and focusing only on the dynamics of the connection between the sources and the loads. This is the approach adopted here.

A similar approach (the use of reduced models) was developed in [4] for linear loads with the stability verified by small-signal analysis. An analogous problem is treated in [5] and [6], where likewise small-signal stability analysis for parallel-connected inverters is applied. Small-signal stability analysis for inverters driving a time-invariant nonlinear load (a controlled ac-dc power converter) is investigated in [7]. Large-signal stability analysis using a Lyapunov function for a different type of reduced model is explored in [8] and [9]. Bifurcation analysis applied to microgrid problems can be seen in [10]. The stability analysis in this paper is verified by using numerical bifurcation techniques, which can be understood as a parametric stability analysis, since one or more of the microgrid parameters are varied in order to construct bifurcation diagrams.

For the microgrid study here, the load is composed by four controlled ac-dc power converters with power factor correction. Assuming an ideal behavior, the rectifier performs similarly to a constant power load (CPL) used in dc networks [11], [12]. The generalization to ac systems can be developed using the PQ theory [13]. One of the problems that arises when a CPL model is used in electrical circuits is the need to have a large capacitor connected in the CPL input terminals. Without this element, the model stability may be compromised. In other words, using a CPL model allows to neglect the internal dynamics of the loads, which in this paper are the ac-dc power converters. This is acceptable if the voltage on the ac-dc power converters input terminals has a large inertia, hence any dynamic linked to the load can be neglected. Usually this is achieved if there is a large capacitor connected in the CPL input terminals, however such large capacitances may not be realistic in practical systems. To overcome this issue, a dynamic CPL model is proposed in this work, which is a first-order low-pass filter applied to the CPL equations. The effect of capacitances on the stability of electrical networks with CPL models can be seen in [14], and also in [15].

A simplified diagram of the microgrid case study here considered is depicted in Fig. 1, whereas Fig. 2 shows the
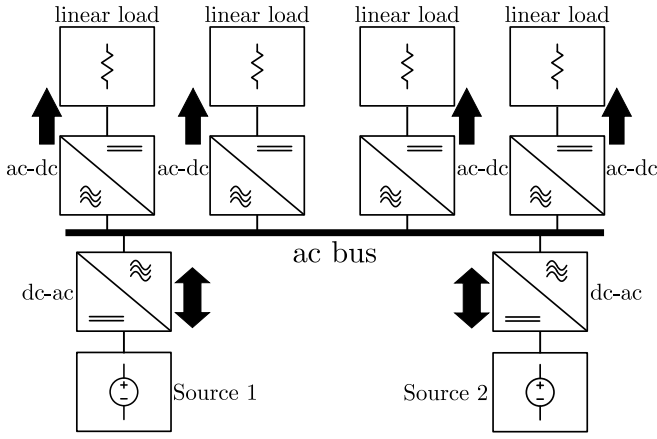
Fig. 1. Load sharing between two dc-ac power converters driving several ac-dc power converters.
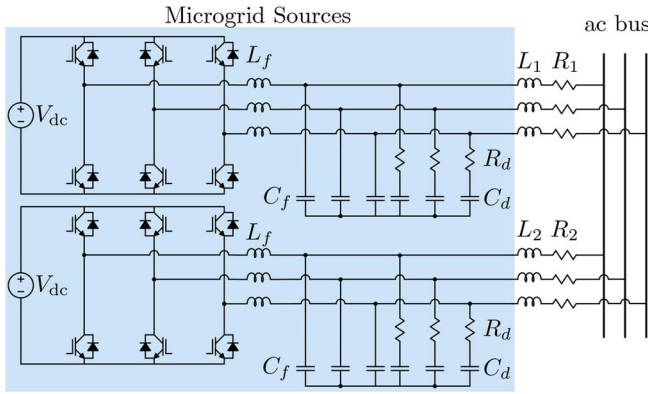

Fig. 2. Microgrid sources (VSIs) highlighting the part of the power converter that is assumed to be an ideal voltage controlled source for the development of the reduced microgrid model.

microgrid sources, which are two parallel-connected voltage-source inverters (VSIs). Moreover, it is assumed that the two inverters are identical, and each one can be modelled as a controlled voltage source in the reduced model. A sub-index k is used to assign each dc-ac power converter throughout the paper with $k \in \{1, 2\}$, and for each ac-dc power converter a subscript $_J$ is used, with $_J \in \{1, 2, 3, 4\}$. All the power converters are controlled through their equivalent three-phase delta states, therefore the input for the $\alpha\beta0$ and dq transforms are the following type: $\{x^{ab}, x^{bc}, x^{ca}\}$, where x can be any variable.

The rest of the paper is organized as follows. The droop equations with the virtual impedance are defined in Section II. The load modeling is presented in Section III, the source modeling and its control is shown in Section IV. The microgrid reduced model is developed in Section V, and the stability analysis and numerical simulations are presented in Sections VI and VII, respectively. The main conclusions of this work are summarized in Section VIII.

II. DROOP CONTROL AND VIRTUAL IMPEDANCE EQUATIONS

The basic inductive droop control loop strategy used for dc-ac power converters operating in parallel is depicted in Fig. 3.
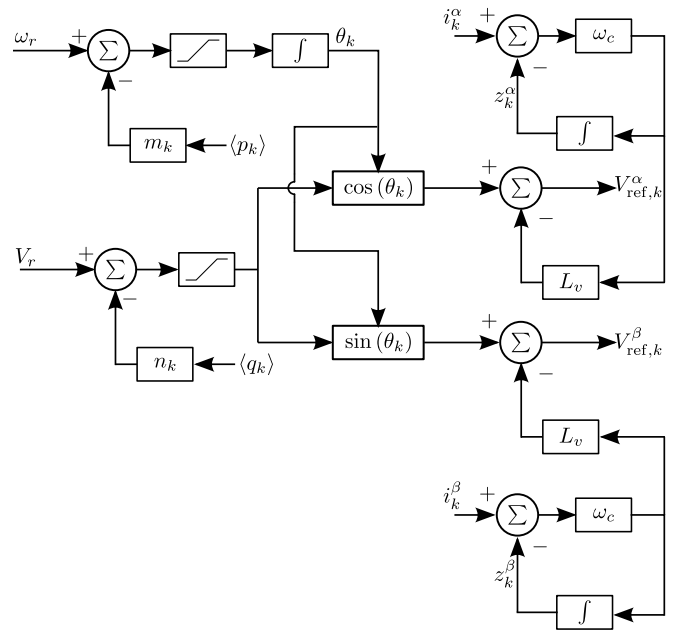

Fig. 3. Inductive droop control diagram with virtual impedance implemented by a washout filter.

The low frequency components of the active, $\langle p_k \rangle$, and reactive, $\langle q_k \rangle$, powers are used to generate the references for the voltage amplitude and frequency, $\omega_k = d\theta_k/dt$, in the droop control.

The inductive droop equations, which are essentially proportional controllers, are given by

$$V_k = \begin{cases} V_{\text{sup}}, & \text{if } V_k \geq V_{\text{sup}} \\ V_r - n_k \langle q_k \rangle, & \text{if } V_{\text{inf}} < V_k < V_{\text{sup}} \\ V_{\text{inf}}, & \text{if } V_k \leq V_{\text{inf}} \end{cases} \quad (1)$$

$$\omega_k = \begin{cases} \omega_{\text{sup}}, & \text{if } \omega_k \geq \omega_{\text{sup}} \\ \omega_r - m_k \langle p_k \rangle, & \text{if } \omega_{\text{inf}} < \omega_k < \omega_{\text{sup}} \\ \omega_{\text{inf}}, & \text{if } \omega_k \leq \omega_{\text{inf}} \end{cases} \quad (2)$$

where $\langle p_k \rangle$ and $\langle q_k \rangle$ are the low frequency inverter output powers (filtered powers); n_k and m_k are the droop gains; V_r and ω_r are the rated values for the peak voltage and the inverter frequency; V_{sup} and V_{inf} are the maximum and minimum values for the voltage amplitude, finally ω_{sup} and ω_{inf} are the maximum and minimum values for the inverter frequency.

Note that the control based on (1) and (2) does not have any reference signal for the active and reactive power because the load defines the amount of power that each source has to dispatch. The system essentially operates in a free operating point regime. The frequency must be synchronized in the steady state, which implies $-m_1 \langle p_1 \rangle = -m_2 \langle p_2 \rangle$, therefore $\langle p_1 \rangle / \langle p_2 \rangle = m_2 / m_1$.

Besides the droop equations, it is usually important to change the inverter output impedance. To achieve this, the voltage reference signal becomes a function of the virtual impedance. Whenever an inductive output impedance is
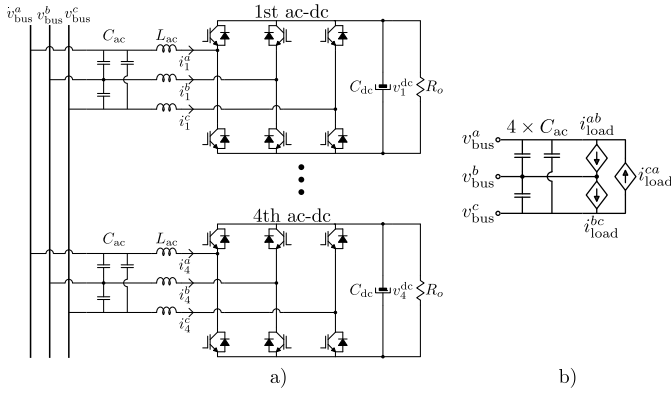
Fig. 4. Controlled ac-dc power converters: a) electrical circuits; and b) equivalent reduced CPL model.

Fig. 5. AC-DC power converter control diagram.

needed, the cross implementation [16]–[18] can be used, which is given by

$$V_{\text{ref},k}^{\alpha} = V_k \cos \theta_k + X_v i_k^{\beta} \tag{3}$$

$$V_{\text{ref},k}^{\beta} = V_k \sin \theta_k - X_v i_k^{\alpha}, \tag{4}$$

with i_k^{α} and i_k^{β}, the VSI output currents, which are the inductors L_1 and L_2 delta equivalent currents (Fig. 2). The inductive reactance is defined as $X_v = \omega_r L_v$, which is a function of ω_r, but not of the frequency ω_k, thus it is always constant.

The presence of an inductive virtual impedance causes an inductive behavior on the inverter output characteristic, where the α dynamic is coupled with the β dynamic. An alternative approach to the cross virtual impedance, where both α and β states are decoupled is the washout filter [3], [19]:

$$V_{\text{ref},k}^{\alpha} = V_k \cos \theta_k - \omega_c L_v \left(i_k^{\alpha} - z_k^{\alpha} \right) \tag{5}$$

$$V_{\text{ref},k}^{\beta} = V_k \sin \theta_k - \omega_c L_v \left(i_k^{\beta} - z_k^{\beta} \right), \tag{6}$$

where $\mathbf{z}_k = [\, z_k^{\alpha} \quad z_k^{\beta} \,]^T$ is the filtered current:

$$\frac{dz_k^{\alpha}}{dt} = \omega_c \left(i_k^{\alpha} - z_k^{\alpha} \right) \tag{7}$$

$$\frac{dz_k^{\beta}}{dt} = \omega_c \left(i_k^{\beta} - z_k^{\beta} \right). \tag{8}$$

The cut-off frequency ω_c has to be higher than ω_k, therefore (7)-(8) can represent a similar virtual inductance compared to (3)-(4), which can be verified based on a steady-state analysis.

III. LOAD DYNAMICS

A. AC-DC Power Converter Modeling and Control

The microgrid load is composed by four identical ac-dc power converters, each one depicted in Fig. 4. Notice the presence of an input capacitor filter from an electro-magnetic interference (EMI) filter, which is a small capacitor filter. The ac-dc power converter control system is represented in Fig. 5, and all the ac-dc parameters are shown in Table I.
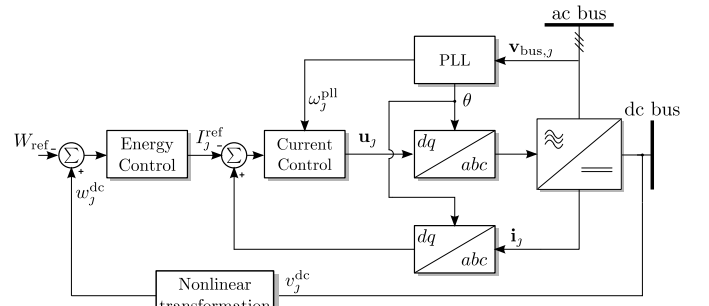
TABLE I
AC-DC POWER CONVERTER PARAMETERS

Parameter	Value	Parameter	Value
L_{ac}	2.5 mH	C_{dc}	500 μF
V_{ref}	500 V	$I_{\max}$	7.5 A
K_1^{pll}	0.296804	K_2^{pll}	5.1802
K_1^i	66.63 Ω	K_2^i	296 088 Ω rad/s
K_1^w	1589 rad/s	K_2^w	988 402 rad^2/s^2
γ	8.0307 W^{-1}s^{-2}	κ	0.011 W^{2}s^4

The $\alpha\beta$ and dq transformations used in this paper are power-invariant, and are defined as

$$\mathbf{T}_{\alpha\beta 0} = \sqrt{\frac{2}{3}} \begin{bmatrix} 0 & -\sqrt{3}/2 & \sqrt{3}/2 \\ 1 & -1/2 & -1/2 \\ 1/\sqrt{2} & 1/\sqrt{2} & 1/\sqrt{2} \end{bmatrix} \tag{9}$$

$$\mathbf{T}_{dq} = \begin{bmatrix} \cos\theta & \sin\theta \\ -\sin\theta & \cos\theta \end{bmatrix}. \tag{10}$$

Each ac-dc power converter is represented by its own set of transformations, therefore there are differences between each angle used in the dq transformation.

The bus voltage is common to all the loads and although each ac-dc power converter control loop is designed independently, a microgrid model for all the loads has to include the possible phase differences between the dq transforms. In order to do that, we define for each ac-dc converter the common bus voltage in dq coordinates as $v_{\text{bus},j}^d$, meaning that the first ac-dc power converter sees the direct-axis bus voltage as $v_{\text{bus},1}^d$; with a similar definition for the other power converters. In order to combine all the ac-dc power converter equations, we use a common dq transform for the bus voltage. Thus adopting the first ac-dc dq angle as a reference for the bus voltages, one obtains:

$$v_{\text{bus},J}^d = v_{\text{bus}}^d \cos \delta_{1J} - v_{\text{bus}}^q \sin \delta_{1J} \tag{11}$$

$$v_{\text{bus},J}^q = v_{\text{bus}}^q \cos \delta_{1J} + v_{\text{bus}}^d \sin \delta_{1J}. \tag{12}$$

The voltages v_{bus}^d and v_{bus}^q are referred to $J = 1$, therefore for $J \in \{2, 3, 4\}$ the bus voltage is a function of the angles δ_{1J}, which are defined as

$$\frac{d\delta_{1J}}{dt} = \omega_1^{\text{pll}} - \omega_J^{\text{pll}}, \tag{13}$$

with ω_J^{pll} the PLL frequency for each power converter. The PLL dynamics are given by a standard

proportional-integral (PI) control applied to the common bus voltage quadrature component in a delta configuration:

$$\omega_J^{\text{pll}} = \omega_r + K_1^{\text{pll}} v_{\text{bus},J}^q + K_2^{\text{pll}} \xi_J^{\text{pll}} \tag{14}$$

$$\frac{d\xi_J^{\text{pll}}}{dt} = v_{\text{bus},J}^q. \tag{15}$$

The control system is applied to the ac-dc power converter in equivalent delta configuration, hence in *dq* coordinates the system becomes

$$3L_{\text{ac}} \frac{di_J^d}{dt} = 3\omega_J^{\text{pll}} L_{\text{ac}} i_J^q - v_J^{\text{dc}} u_J^d + v_{\text{bus},J}^d \tag{16}$$

$$3L_{\text{ac}} \frac{di_J^q}{dt} = -3\omega_J^{\text{pll}} L_{\text{ac}} i_J^d - v_J^{\text{dc}} u_J^q + v_{\text{bus},J}^q \tag{17}$$

$$C_{\text{dc}} \frac{dv_J^{\text{dc}}}{dt} = u_J^d i_J^d + u_J^q i_J^q - \frac{v_J^{\text{dc}}}{R_o}, \tag{18}$$

where i_J^d, i_J^q are the direct and quadrature delta equivalent L_{ac} inductor currents, respectively; v_J^{dc} is the dc voltage; and R_o is the load resistance.

The ac-dc power converter model can also be described by

$$L_{\text{ac}}^e \frac{di_J^d}{dt} = \omega_J^{\text{pll}} L_{\text{ac}}^e i_J^q - h_J^d + v_{\text{bus},J}^d \tag{19}$$

$$L_{\text{ac}}^e \frac{di_J^q}{dt} = -\omega_J^{\text{pll}} L_{\text{ac}}^e i_J^d - h_J^q + v_{\text{bus},J}^q \tag{20}$$

$$\frac{dw_J^{\text{dc}}}{dt} = h_J^d i_J^d + h_J^q i_J^q - \mu w_J^{\text{dc}}, \tag{21}$$

by applying the following nonlinear transformations $v_J^{\text{dc}} u_J^d = h_J^d$, $v_J^{\text{dc}} u_J^q = h_J^q$, and $w_J^{\text{dc}} = (1/2) C_{\text{dc}} v_J^{\text{dc}} v_J^{\text{dc}}$, where $\mu = 2/(R_o C_{\text{dc}})$, and $L_{\text{ac}}^e = 3L_{\text{ac}}$.

The current control loop law given by [20]:

$$h_J^d = v_{\text{bus},J}^d + \omega_J^{\text{pll}} L_{\text{ac}}^e i_J^q + K_1^i \left(i_J^d - I_J^{\text{ref}} \right) + K_2^i \xi_J^d \tag{22}$$

$$h_J^q = v_{\text{bus},J}^q - \omega_J^{\text{pll}} L_{\text{ac}}^e i_J^d + K_1^i i_J^q + K_2^i \xi_J^q, \tag{23}$$

with

$$\frac{d\xi_J^d}{dt} = i_J^d - I_J^{\text{ref}} \tag{24}$$

$$\frac{d\xi_J^q}{dt} = i_J^q, \tag{25}$$

is based on the feedback linearization technique.

The ac-dc power converter dynamics with the current control law (22)-(25) become

$$L_{\text{ac}}^e \frac{di_J^d}{dt} = -K_1^i i_J^d - K_2^i \xi_J^d + K_1^i I_J^{\text{ref}} \tag{26}$$

$$L_{\text{ac}}^e \frac{di_J^q}{dt} = -K_1^i i_J^q - K_2^i \xi_J^q \tag{27}$$

$$\frac{dw_J^{\text{dc}}}{dt} = v_{\text{bus},J}^d i_J^d + v_{\text{bus},J}^q i_J^q - \mu w_J^{\text{dc}}$$
$$+ i_J^d \left[K_1^i \left(i_J^d - I_J^{\text{ref}} \right) + K_2^i \xi_J^d \right]$$
$$+ i_J^q \left(K_1^i i_J^q + K_2^i \xi_J^q \right). \tag{28}$$

The equilibrium point for the system states is: $i_J^d \to I_J^{\text{ref}}$, $i_J^q \to 0$, $\xi_J^d \to 0$ and $\xi_J^q \to 0$.

The outer control loop is designed assuming that the dynamics of w_J^{dc} evolve in a slower time-scale when compared to the currents i_J^d and i_J^q. Thus, the current control loop is assumed to be operating in steady-state, and (28) becomes

$$\frac{dw_J^{\text{dc}}}{dt} \approx v_{\text{bus},J}^d I_J^{\text{ref}} - \mu w_J^{\text{dc}}. \tag{29}$$

By applying the same feedback linearization technique to (29), I_J^{ref} is calculated as

$$I_J^{\text{ref}} = \begin{cases} \dfrac{\hat{\mu}_J w_J^{\text{dc}} - K_1^w \epsilon_J^{\text{dc}} - K_2^w \xi_J^{\text{dc}}}{v_{\text{bus},J}^d}, & \text{if } i_J^d < I_{\text{max}} \\ I_{\text{max}}, & \text{if } i_J^d > I_{\text{max}} \end{cases} \tag{30}$$

with $\epsilon_J^{\text{dc}} = w_J^{\text{dc}} - W_{\text{ref}}$, W_{ref} being the reference signal, $W_{\text{ref}} = (1/2) C_{\text{dc}} V_{\text{ref}}^2$, and $\hat{\mu}_J = \rho_J + \sigma_J$ the load estimation, which is designed assuming the load μ is a constant unknown parameter by applying the Immersion & Invariance (I&I) nonlinear adaptive technique [21]. The static part of the estimation is chosen to be $\sigma_J = -\gamma w_J^{\text{dc}}$, with γ the estimation gain, whereas the dynamic part of the estimation is

$$\frac{d\rho_J}{dt} = -\gamma \left(K_1^w \epsilon_J^{\text{dc}} + K_2^w \xi_J^{\text{dc}} \right) - \frac{w_J^{\text{dc}}}{\kappa} \epsilon_J^{\text{dc}}, \tag{31}$$

with ξ_J^{dc} the output of the integral action,

$$\frac{d\xi_J^{\text{dc}}}{dt} = \epsilon_J^{\text{dc}}. \tag{32}$$

The energy control loop given by (29)-(32), see Fig. 5, is based on a PI control with a feedforward term ($\hat{\mu}_J w_J^{\text{dc}}$), where the parameter μ has to be estimated since the load is not measured. Therefore, to apply this feedforward technique, the I&I estimation is used. The advantage of this scheme compared to a PI controller is that load variations do not affect the linear part of the voltage control loop dynamics. Only the constants K_1^w, K_2^w, γ, and W_{ref} are presented in the jacobian matrix. Ideally, the load μ only affects the system initial conditions.

The set (29)-(32) can be proved stable in the sense of Lyapunov by defining the following candidate Lyapunov function

$$\mathcal{H} = \frac{1}{2} \left(w_J^{\text{dc}} - W_{\text{ref}} \right)^2 + \frac{\kappa}{2} \left(\rho_J + \sigma_J - \mu \right)^2 + \frac{K_2^w}{2} \left(\xi_J^{\text{dc}} \right)^2 \tag{33}$$

with

$$\frac{d\mathcal{H}}{dt} = -K_1^w \left(w_J^{\text{dc}} - W_{\text{ref}} \right)^2 - \kappa \gamma w_J^{\text{dc}} \left(\rho_J + \sigma_J - \mu \right)^2. \tag{34}$$

As $w_J^{\text{dc}} \in \mathbb{R}^+$, (34) is negative semidefinite, using LaSalle's invariance principle, it can be shown that this system is asymptotically stable. The current control loop was assumed to be in steady state for the energy control loop dynamic stability, thus this analysis is only local. The constant κ is used only to make the physical dimension of $\mathcal{H}$ consistent. The complete ac-dc power converter control system proposed makes the current dynamics approximately linear for fast dynamics, and the energy dynamics become approximately linear for slower dynamics, but the overall system is still nonlinear.

These control laws must be implemented through a discrete-version, which can be done through the zero-order hold (ZOH) discretization. Sampling the ac-dc power converter states, the energy controller dynamics (31)-(32) becomes a double-integrator system given by

$$\rho_J[n] = \rho_J[n-1] + T_a w_J^{dc}[n-1]\epsilon_J^{dc}[n-1]$$
$$- T_a \gamma \left\{ K_1^w \epsilon_J^{dc}[n-1] + K_2^w \xi_J^{dc}[n-1] \right.$$
$$\left. + K_2^w T_a \epsilon_J^{dc}[n-1] \right\} \tag{35}$$

$$\xi_J^{dc}[n] = \xi_J^{dc}[n-1] + T_a \epsilon_J^{dc}[n-1], \tag{36}$$

where T_a is the sampling period.

B. Reduced Load Model

In order to develop a reduced load model, the ac-dc power converter is simplified based on how the control loops behave. There are two main operation regions for the ac-dc power converter: i) whenever the energy and current control loop are working properly, the ac-dc power converter extracts constant active power from the common bus; and ii) when the energy control loop saturates but the current control loop is operating normally, the ac-dc power converters behave like current sources connected to the common bus. If an ideal power factor correction (PFC) is assumed, then the reactive power is zero in both operating modes.

The equilibrium value for (28) is

$$I_J^{ref} \rightarrow \frac{\mu w_J^{dc}}{v_{bus,J}^d} = \frac{\left(v_J^{dc}\right)^2 / R_o}{v_{bus,J}^d} = \frac{P_J}{v_{bus,J}^d}, \tag{37}$$

and as the control ensures tracking, $v_J^{dc} v_J^{dc} \rightarrow V_{ref}^2$, for a constant R_o, each ac-dc power converter withdraws a constant power ($P_J = V_{ref}^2 / R_o$) from the bus terminals. Neglecting the dynamics on I_J^{ref}, (26)-(27) becomes

$$L_{ac}^e \frac{di_J^d}{dt} = -K_1^i i_J^d + K_1^i \frac{P_J}{v_{bus,J}^d} - K_2^i \xi_J^d \tag{38}$$

$$L_{ac}^e \frac{di_J^q}{dt} = -K_1^i i_J^q - K_2^i \xi_J^q. \tag{39}$$

The reduced load model must capture the correct equilibrium but with fewer states, thus assuming $\xi_J^d \rightarrow 0$ and $\xi_J^q \rightarrow 0$ when $i_J^d \rightarrow I_J^{ref}$, $i_J^q \rightarrow 0$ in (26)-(27), the load model dimension decreases. Also, the load model must incorporate all the four ac-dc power converters, therefore the total load current can be defined as

$$i_{load}^d = i_1^d + \sum_{J=2}^{4} i_J^d \cos\delta_{1J} + i_J^q \sin\delta_{1J} \tag{40}$$

$$i_{load}^q = i_1^q + \sum_{J=2}^{4} -i_J^d \sin\delta_{1J} + i_J^q \cos\delta_{1J}. \tag{41}$$

The same stability from the full ac-dc power converter dynamics can be achieved if an equivalent load dynamic is defined

$$\frac{di_{load}^d}{dt} = -\lambda i_{load}^d + \lambda \frac{P_o}{v_{bus}^d} \tag{42}$$

$$\frac{di_{load}^q}{dt} = -\lambda i_{load}^q. \tag{43}$$

λ is the inverse of the equivalent load time-constant, and P_o is the sum of the four ac-dc power converters powers, $P_o = \sum P_J$. An important remark about (42)-(43), is that these equations represent a proposed model, hence the full ac-dc power converter model stability properties can be mapped to a smaller system. The concept of defining a low-pass filter applied to the equilibrium point as a way to model a power converter was used in [9], but in a different problem.

Ideally, it is expected that $\omega_i > \lambda > \omega_w$, where $\omega_i = \sqrt{K_2^i / L_{ac}^e}$ is the current control loop crossover frequency. As for ω_w, notice that (29)-(32) is a third-order system and the frequency of the dominant eigenvalue can be selected as a lower bound on λ. The control delay together with the PWM delay can also have a deep impact on λ, and these phenomena can make the process of finding a value for λ a bit more complicated. Notice that the way the sources are modeled can also impact on how to choose λ, i.e., if the sources are an instantaneous system or a dynamical one, choosing a value for λ can be challenging. It is a trial and error procedure to find a value for λ.

When the power P_J of each ac-dc power converter increases enough to saturate (30), the equivalent load dynamic changes to

$$\frac{di_{load}^d}{dt} = -\lambda i_{load}^d + \lambda I_{max} \tag{44}$$

$$\frac{di_{load}^q}{dt} = -\lambda i_{load}^q, \tag{45}$$

thus becoming a current source. I_{max} is four times the value used in (30), therefore $I_{max} = 30$ A. The transition from (42) to (44) must be continuous, thus

$$V_{th} = \frac{P_o}{I_{max}}, \tag{46}$$

which is the v_{bus}^d voltage value when the load changes its characteristic from CPL to current source, therefore when $v_{bus}^d > V_{th}$ the load is given by (42)-(43) and when $v_{bus}^d < V_{th}$ the load model becomes (44)-(45).

As the four ac-dc power converters are modelled as one equivalent element, the PLL can also be given in terms of one equivalent PLL:

$$\omega_{load} = \omega_r + K_1^{pll} v_{bus}^q + K_2^{pll} \xi^{pll} \tag{47}$$

$$\frac{d\xi^{pll}}{dt} = v_{bus}^q. \tag{48}$$

An important remark about this reduced load model, while the ac-dc power converter control system presented is nonlinear, different types of controller can reach the same reduced load model as long as the dc voltage is regulated to a constant reference and the input ac currents only draws active power from the common bus voltage. Therefore this approach to model an ac-dc power converter is a bit more general that it might seem.

The capacitance C_{ac} is part of the reduced load model, thus including the four capacitances for each ac-dc power converters, the equivalent bus capacitance is $C_o = 4 \times C_{ac}$. The bus

TABLE II
DC-AC POWER CONVERTERS PARAMETERS

Parameter	Value	Parameter	Value
L_f	460 μH	m_k	0.0001
L_k	230 μH	n_k	0.000173205
R_d	12 Ω	ω_f	62.84 rad/s
R_k	10 mΩ	ω_c	6284 rad/s
C_o	4 μF	V_{dc}	380 V
C_d	2 μF	V_r	330 V
C_f	4 μF	V_{sup}	380 V
ω_r	377 rad/s	V_{inf}	247 V
ω_{sup}	410 rad/s	ω_{inf}	345 rad/s
K_1	0.139876	K_2	7.24638
K_p	8.042	X_v	0.03 Ω

voltage dynamic in $\alpha\beta$ coordinates is

$$C_o \frac{d\mathbf{v}_{bus}}{dt} = \mathbf{i}_1 + \mathbf{i}_2 - \mathbf{i}_{load} \tag{49}$$

with $\mathbf{i}_k = [\, i_k^\alpha \quad i_k^\beta \,]^T$, $\mathbf{i}_{load} = [\, i_{load}^\alpha \quad i_{load}^\beta \,]^T$, and $\mathbf{v}_{bus} = [\, v_{bus}^\alpha \quad v_{bus}^\beta \,]^T$.

IV. SOURCE DYNAMICS

A. DC-AC Power Converter Modeling and Control

The inverter topologies are depicted in Fig. 2 with the shaded region being the parts of the power converter that are modeled as voltage sources in the reduced model. In $\alpha\beta$ coordinates, the inverter model for a delta equivalent circuit is given by

$$3L_f \frac{d\mathbf{x}_k}{dt} = V_{dc}\mathbf{u}_k - \mathbf{v}_k \tag{50}$$

$$\frac{C_f}{3} \frac{d\mathbf{v}_k}{dt} = \mathbf{x}_k - \mathbf{i}_k - \frac{\mathbf{v}_k - \mathbf{y}_k}{3R_d} \tag{51}$$

$$\frac{C_d}{3} \frac{d\mathbf{y}_k}{dt} = \frac{\mathbf{v}_k - \mathbf{y}_k}{3R_d} \tag{52}$$

$$3L_k \frac{d\mathbf{i}_k}{dt} = -3R_k\mathbf{i}_k + \mathbf{v}_k - \mathbf{v}_{bus}, \tag{53}$$

with $\mathbf{x}_k = [\, x_k^\alpha \quad x_k^\beta \,]^T$, $\mathbf{v}_k = [\, v_k^\alpha \quad v_k^\beta \,]^T$, $\mathbf{y}_k = [\, y_k^\alpha \quad y_k^\beta \,]^T$, and $\mathbf{u}_k = [\, u_k^\alpha \quad u_k^\beta \,]^T$. The inverter states are defined as: $\mathbf{x}_k$, representing the equivalent L_f inductor delta currents; $\mathbf{v}_k$ the voltages on the delta equivalent capacitors C_f; $\mathbf{y}_k$ the voltages on the delta equivalent capacitors C_d; and $\mathbf{i}_k$ the inverter output delta equivalent currents. The dc-ac power converter parameters are given in Table II.

The inverter control loop can be designed assuming a fast inner current control loop and a slow outer voltage control loop. For the inner loop, the duty cycle can be chosen as

$$\mathbf{u}_k = \frac{\mathbf{v}_k - K_p(\mathbf{x}_k - \mathbf{x}_{ref,k})}{V_{dc}}, \tag{54}$$

with $\mathbf{x}_{ref,k}$ the outer loop output signal and K_p the proportional gain.

The voltage control loop control law is given by

$$\mathbf{x}_{ref,k} = \mathbf{i}_k - K_1\boldsymbol{\epsilon}_k - K_2\boldsymbol{\xi}_k, \tag{55}$$

with the voltage control loop error defined as

$$\boldsymbol{\epsilon}_k = \mathbf{v}_k - \mathbf{V}_{ref,k} \tag{56}$$

and the resonant controller given by

$$\frac{d\boldsymbol{\xi}_k}{dt} = \omega_k\boldsymbol{\eta}_k + \boldsymbol{\epsilon}_k \tag{57}$$

$$\frac{d\boldsymbol{\eta}_k}{dt} = -\omega_k\boldsymbol{\xi}_k, \tag{58}$$

where $\boldsymbol{\xi}_k = [\, \xi_k^\alpha \quad \xi_k^\beta \,]^T$ and $\boldsymbol{\eta}_k = [\, \eta_k^\alpha \quad \eta_k^\beta \,]^T$. The inverter control system is given by (54)-(58).

The discrete-version of the resonant controller is given by

$$\boldsymbol{\xi}_k[n] = \boldsymbol{\xi}_k[n-1]\cos\omega_k T_a + \boldsymbol{\eta}_k[n-1]\sin\omega_k T_a$$
$$+ \frac{\boldsymbol{\epsilon}_k}{\omega_k}\sin\omega_k T_a \tag{59}$$
$$\boldsymbol{\eta}_k[n] = \boldsymbol{\eta}_k[n-1]\cos\omega_k T_a - \boldsymbol{\xi}_k[n-1]\sin\omega_k T_a$$
$$+ \frac{\boldsymbol{\epsilon}_k}{\omega_k}(\cos\omega_k T_a - 1), \tag{60}$$

where

$$\cos\omega_k T_a = \cos\theta_k[n]\,\cos\theta_k[n-1]$$
$$+ \sin\theta_k[n]\,\sin\theta_k[n-1] \tag{61}$$
$$\sin\omega_k T_a = \sin\theta_k[n]\,\cos\theta_k[n-1]$$
$$- \cos\theta_k[n]\,\sin\theta_k[n-1], \tag{62}$$

with T_a the sampling period. Notice that in this discrete-version of the controller, the frequency ω_k is measured at each cycle differently of the usual version where it is constant.

The dc-ac power converter dynamic with the proposed control becomes

$$L_f^e \frac{d\mathbf{x}_k}{dt} = -K_p\mathbf{x}_k + K_p(\mathbf{i}_k - K_1\boldsymbol{\epsilon}_k - K_2\boldsymbol{\xi}_k) \tag{63}$$

$$\frac{d\boldsymbol{\xi}_k}{dt} = \boldsymbol{\epsilon}_k + \omega_k\boldsymbol{\eta}_k \tag{64}$$

$$\frac{d\boldsymbol{\eta}_k}{dt} = -\omega_k\boldsymbol{\xi}_k \tag{65}$$

$$C_f^e \frac{d\mathbf{v}_k}{dt} = \mathbf{x}_k - \mathbf{i}_k - \frac{\mathbf{v}_k - \mathbf{y}_k}{R_d^e} \tag{66}$$

$$C_d^e \frac{d\mathbf{y}_k}{dt} = \frac{\mathbf{v}_k - \mathbf{y}_k}{R_d^e} \tag{67}$$

$$L_k^e \frac{d\mathbf{i}_k}{dt} = -R_k^e\mathbf{i}_k + \mathbf{v}_k - \mathbf{v}_{bus}, \tag{68}$$

with $L_f^e = 3L_f$, $C_f^e = C_f/3$, $C_d^e = C_d/3$, $R_d^e = 3R_d$, $L_k^e = 3L_k$ and $R_k^e = 3R_k$.

To choose the inverter control system gains, the reduced load model can be used as a benchmark for the dc-ac power converter control system, as depicted in Fig. 6. The stability analysis for the inverters must be done using *dq* coordinates.

An iterative process is adopted to find an optimal value of the parameter λ. In order to do so, the VSIs control gains based on an ad hoc procedure are first chosen, and, second, one can proceed to verify the inverters stability by simulation, and at the same time adjusting λ. Based on this simulation, it is possible to find a value of λ that makes the reduced model match the same stability found for a simulation based on switching models. More accurate analyses can be made for the
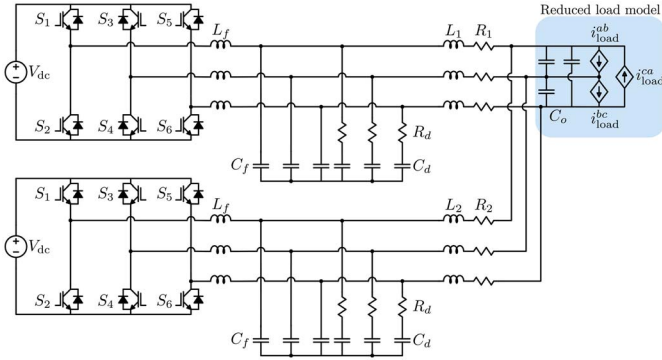
Fig. 6. Configuration to test the VSI control system gains K_1, K_2 and K_p using the reduced load model.

controller gains based on bifurcation diagrams by varying the load power, which helps to see how close or how far from the instability is the inverter.

The VSI reference signals in dq coordinates are given by

$$V^d_{\text{ref},k} = V_k - \omega_c L_v\left(i^d_k - z^d_k\right) \qquad (69)$$

$$V^q_{\text{ref},k} = -\omega_c L_v\left(i^q_k - z^q_k\right), \qquad (70)$$

with the instantaneous output powers defined by the PQ theory:

$$p_k = V_k i^d_k - \omega_c L_v \|\mathbf{i}_k\|^2 + \omega_c L_v\left(i^d_k z^d_k + i^q_k z^q_k\right) \qquad (71)$$

$$q_k = -V_k i^q_k - \omega_c L_v\left(i^q_k z^d_k - i^d_k z^q_k\right), \qquad (72)$$

where $\|\mathbf{i}_k\|^2 = i^d_k i^d_k + i^q_k i^q_k$. The low-frequency powers together with the washout filter, in dq coordinates, are given by

$$\frac{d\langle p_k\rangle}{dt} = -\omega_f(\langle p_k\rangle - p_k) \qquad (73)$$

$$\frac{d\langle q_k\rangle}{dt} = -\omega_f(\langle q_k\rangle - q_k) \qquad (74)$$

$$\frac{dz^d_k}{dt} = \omega_k z^q_k + \omega_c\left(i^d_k - z^d_k\right) \qquad (75)$$

$$\frac{dz^q_k}{dt} = -\omega_k z^d_k + \omega_c\left(i^q_k - z^q_k\right). \qquad (76)$$

The VSI dynamic average model is given by the equivalent (63)-(68) in dq and (73)-(76), which gives 16 nonlinear differential equations for each inverter. Notice that there is a difference between the dq angles for the VSIs and the equivalent load, which can be defined as $\phi_k = \theta_k - \theta_{\text{load}}$, therefore

$$\frac{d\phi_k}{dt} = -m_k\langle p_k\rangle - K^{\text{pll}}_1 v^q_{\text{bus}} - K^{\text{pll}}_2 \xi^{\text{pll}}. \qquad (77)$$

Using θ_{load} for the common bus voltage (49) dq transform, the bus voltage becomes

$$C_o\frac{dv^d_{\text{bus}}}{dt} = \omega_{\text{load}} C_o v^q_{\text{bus}} + i^d_1 \cos\phi_1 - i^q_1 \sin\phi_1$$
$$+ i^d_2 \cos\phi_2 - i^q_2 \sin\phi_2 - i^d_{\text{load}} \qquad (78)$$

$$C_o\frac{dv^q_{\text{bus}}}{dt} = -\omega_{\text{load}} C_o v^d_{\text{bus}} + i^d_1 \sin\phi_1 + i^q_1 \cos\phi_1$$
$$+ i^d_2 \sin\phi_2 + i^q_2 \cos\phi_2 - i^q_{\text{load}}. \qquad (79)$$
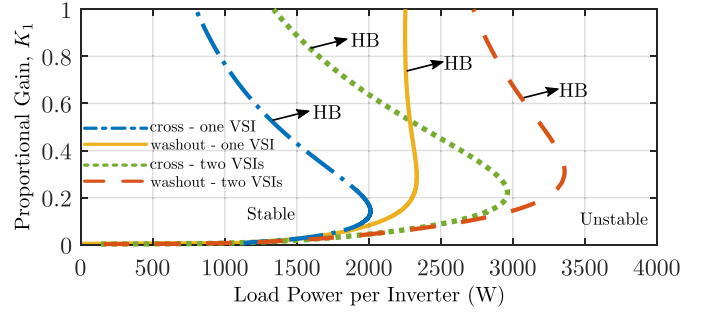

Fig. 7. Stability diagram on the plane-$\{P_o, K_1\}$ for the dc-ac power converter with P_o divided by the number of sources.
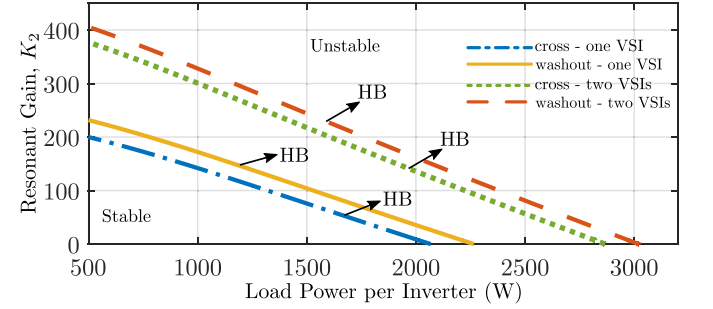

Fig. 8. Stability diagram on the plane-$\{P_o, K_2\}$ for the dc-ac power converter with P_o divided by the number of sources.

The reduced load model is given by (42)-(43), and (77)-(79), which gives seven differential equations. Together with both VSIs, the configuration from Fig. 6 totalizes 39 nonlinear differential equations. For the cross virtual impedance implementation, small modifications must be made to the equations shown.

Using MATCONT [22] and XPP-AUTO [23], [24], both numerical bifurcation analysis packages, one can study the VSI local stability by varying the reduced load power P_o and plot the region where the dc-ac power converters are stable. A value of $\lambda = 7150$ rad/s gives a similar stability when the four ac-dc power converters are substituted by the reduced load model, hence Figs. 7–10 show how to choose the gains K_1, K_2, K_p and X_v, respectively. It is interesting to compare when both dc-ac power converters are working and when only one of them is active. Ideally, when both VSIs are activated the maximum load power where the system is stable should be twice the power of one source. In order to compare both situations, the curves are calculated for the load power per inverter, which means for the system with only one inverter the load power is P_o, and when both inverters are on, the power is $P_o/2$.

The curves labelled as HB in Figs. 7–10 denote a Hopf bifurcation, where the stability of the inverter changes from a stable equilibrium point to an unstable equilibrium point and, at the same time, arising a stable limit cycle, which makes the system to oscillate in dq coordinates. The jacobian matrix of the linearized VSI model calculated at this point has two eigenvalues on the imaginary axis, that pass to the right side of the complex plane when the power P_o is increased. Below and to the left of these curve the system is stable otherwise it
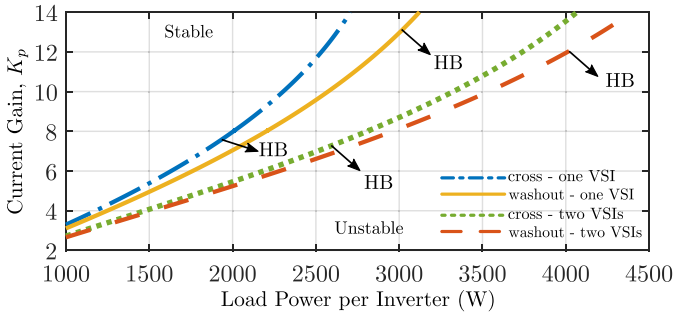
Fig. 9. Stability diagram on the plane-$\{P_o, K_p\}$ for the dc-ac power converter with P_o divided by the number of sources.
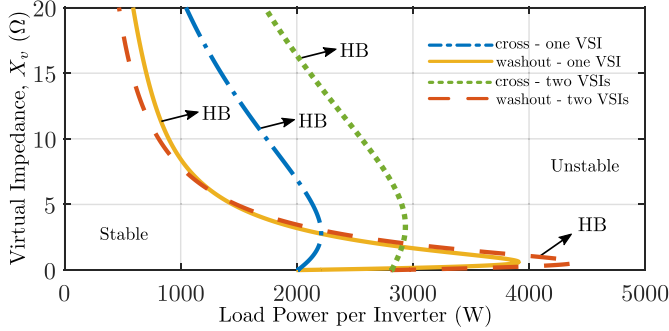

Fig. 10. Stability diagram on the plane-$\{P_o, X_v\}$ for the dc-ac power converter with P_o divided by the number of sources.

is unstable. Notice that when there are more VSIs operating in parallel, each power converter can process more power because the stability region increase 1 kW per inverter. One advantage of using only one inverter for the design of the controller gains is the reduced number of equations, from 39 it goes to 23 non-linear differential equations, and based on Figs. 7–9, it gives a worst-case scenario. For the virtual impedance, the situation is more complicated, as there are values for X_v where the stability per power inverter decreases. Finally, for low values of K_1, K_2 and K_p, both virtual impedances give similar stability results. Increasing beyond $K_1 > 0.2$, the VSI duty cycle harmonic contents start to increase, thus in practical terms both virtual impedances have similar stability properties.

B. Reduced Source Model

The VSI full model is helpful for the design of the control system. However, in the analysis of the interaction between sources in an islanded microgrid, the number of equations becomes too large even for only a few inverters operating in parallel. To overcome this problem, a reduced source model is developed. Equation (68) can be rewritten as

$$L_k^e \frac{d\mathbf{i}_k}{dt} = -R_k^e \mathbf{i}_k + \boldsymbol{\epsilon}_k + \mathbf{V}_{\text{ref},k} - \mathbf{v}_{\text{bus}}, \qquad (80)$$

and assuming the inverter internal dynamics ($\mathbf{x}_k$, $\boldsymbol{\xi}_k$, $\boldsymbol{\eta}_k$, $\mathbf{v}_k$, and $\mathbf{y}_k$) are stable, then $\boldsymbol{\epsilon}_k \to 0$ and the reduced model for the dc-ac source dynamics can be used, as follows:

$$L_k^e \frac{d\mathbf{i}_k}{dt} \cong -R_k^e \mathbf{i}_k + \mathbf{V}_{\text{ref},k} - \mathbf{v}_{\text{bus}}. \qquad (81)$$
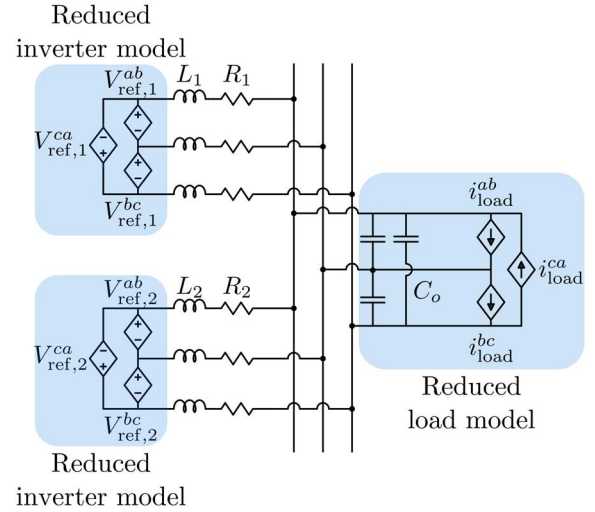

Fig. 11. Equivalent circuit representing the equations of the reduced model for the microgrid under study: two parallel-connected inverters and an equivalent CPL.

This procedure was developed in [4] and can give the correct system stability as long as K_1 and K_2 are properly selected, for instance as shown in Figs. 7–10. The complete dc-ac power converter stability is a function of $\mathbf{x}_k$, $\boldsymbol{\xi}_k$, $\boldsymbol{\eta}_k$, $\mathbf{v}_k$, and $\mathbf{y}_k$, therefore if the inverter becomes unstable due to its internal dynamics, the reduced source model cannot capture this type of behavior.

If a reduced source model, given by (81) and (3)-(4) is used, then an appropriate value for λ would be $\lambda = 1800$ rad/s. Nevertheless, if (81) is used with (5)-(6), $\lambda = 6600$ rad/s. The reason for this difference is the lack of any differential equation for the source model when the cross virtual impedance is used, i.e., (3)-(4) are instantaneous magnitudes, whereas (5)-(6) have a low-pass filter due to the washout filter.

V. REDUCED MICROGRID MODEL

The equivalent circuit representing the equations of the reduced model for two parallel-connected inverters and an equivalent CPL is depicted in Fig. 11. In addition to the output inductance filter (L_1^e and L_2^e), the sources are modeled by their approximated steady state characteristics.

Applying the *dq* transformation to (81), i.e., $i_k^d = \cos\theta_k i_k^\alpha + \sin\theta_k i_k^\beta$, $i_k^q = -\sin\theta_k i_k^\alpha + \cos\theta_k i_k^\beta$, the current dynamics become

$$L_k^e \frac{di_k^d}{dt} = \omega_k L_k^e i_k^q - R_k^e i_k^d + V_{\text{ref},k}^d$$
$$- v_{\text{bus}}^d \cos\phi_k - v_{\text{bus}}^q \sin\phi_k \qquad (82)$$
$$L_k^e \frac{di_k^q}{dt} = -\omega_k L_k^e i_k^d - R_k^e i_k^q + V_{\text{ref},k}^q$$
$$+ v_{\text{bus}}^d \sin\phi_k - v_{\text{bus}}^q \cos\phi_k. \qquad (83)$$

The overall microgrid reduced model is given by four dynamic equations corresponding to the line currents (82)-(83), the bus voltage dynamic (78)-(79), the load dynamic (42)-(43), the two angle equations with the PLL
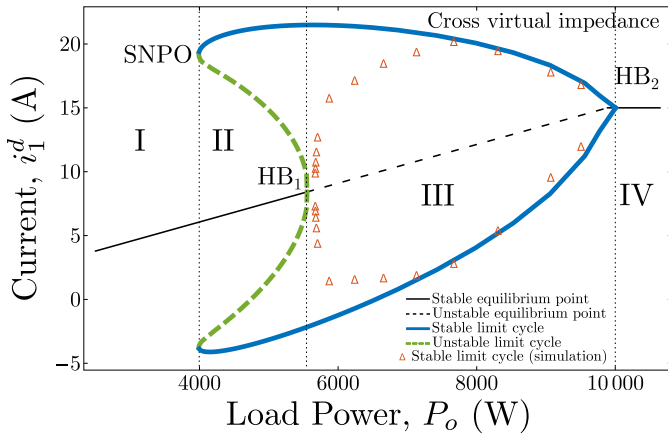
Fig. 12. Bifurcation diagram in the $\{P_o, i_1^d\}$-plane for $\lambda = 1800$ rad/s, $X_v = 0.03$ Ω, and with the virtual impedance given by (3)-(4).
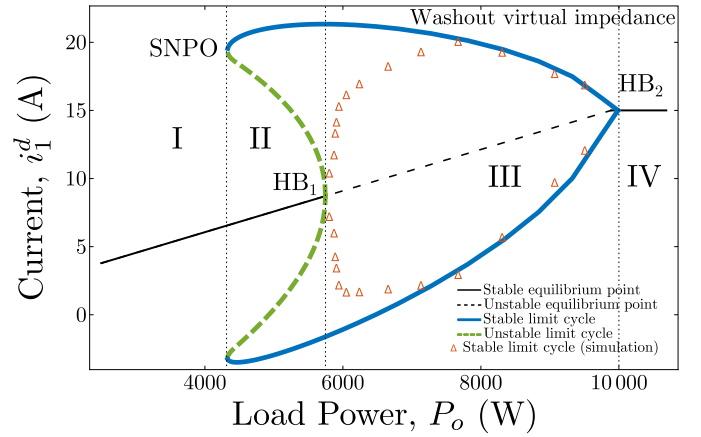

Fig. 13. Bifurcation diagram in the $\{P_o, i_1^d\}$-plane for $\lambda = 6600$ rad/s, $X_v = 0.03$ Ω, and with the virtual impedance given by (5)-(6).

integral action (77) and (48), the four filtered power equations (73)-(74), and the four washout filter dynamics (75)-(76), totaling 19 nonlinear differential equations. When the virtual impedance is given by (3)-(4), small modifications must be made in the microgrid reduced model, and the total number of differential equations becomes 15.

VI. NUMERICAL BIFURCATION ANALYSIS

In this section standard bifurcation techniques [25] are used to analyze the stability of the reduced microgrid model. The reduced model has to capture the main dynamic behavior of the full model, with the equilibrium points and their stability as the main characteristics to be preserved. Since the load is modeled as a CPL with a low-pass filter, it is easy to choose the filter frequency that matches the complete microgrid model stability. Unfortunately, global dynamic behavior may not be well modeled by the reduced model since the full model behavior can be sensitive to the sources and load control loop dynamics, and even to some switching characteristics of the power converters.

Using XPP-AUTO it is possible to plot bifurcation diagrams by varying one of the microgrid parameters. For instance, Fig. 12 shows a bifurcation diagram for the current i_1^d when the load power P_o varies using the cross virtual impedance implementation, and Fig. 13 shows the same bifurcation diagram, but for the washout virtual impedance. The other system variables have similar bifurcation diagrams, thus, here to be concise, the focus is only on the current i_1^d.

When the load power consumption is low, the system equilibrium is stable, but when operating close to 5.5 kW, the reduced model exhibits two eigenvalues crossing the imaginary axis, which implies a Hopf bifurcation (HB$_1$). For the microgrid of this study the appearance of this bifurcation is due to the load type, and CPL models typically undergo a subcritical Hopf bifurcation [15]. A subcritical Hopf bifurcation gives rise to an unstable limit cycle around the stable equilibrium point and this implies that the stable equilibrium point have a region of attraction. This unstable limit cycle collapses with a stable limit cycle close to $P_o = 4$ kW in a global bifurcation called as saddle-node of periodic orbits (SNPO). This bifurcation is due

to the discontinuity of the load model, see (42)-(45). The stable limit cycle disappears into a stable equilibrium point close to 10 kW. This second Hopf bifurcation (HB$_2$), now supercritical, is defined by the load parameter (46), and it happens because the load current increases until the current control loop of the ac-dc power converters saturates.

There are four main operation regions in the microgrid case study proposed in this paper, as depicted in Fig. 12: i) Region I is when the load is behaving like a CPL and the equilibrium point is stable; ii) Region II is between the SNPO and the HB$_1$ points where two limit cycles coexist (one inner unstable and another one stable around it); iii) Region III is when there is only one stable limit cycle around one unstable equilibrium point; and iv) Region IV is when the load current saturates and the system has again a stable equilibrium point.

In order to validate the analytical results obtained with the reduced microgrid model, some simulations were performed using PSIM software for the full switching microgrid model (Fig. 1). In the PSIM simulation, the dynamics of all the power converters in taken into account, and the controllers are implemented in the discrete-time domain.

Fig. 12 displays these simulation results superposed on the bifurcation diagram where the symbols Δ stand for the amplitude of the stable limit cycle, i.e., the positive and negative peak values of the oscillations on the current i_1^d.

It can be observed in Figs. 12–13 that the Region II does not exist when using the switching ac-dc power converter models, therefore the reduced load model, although it reproduces the correct local stability of the system, it does not capture this global phenomenon correctly. Region III, where the system is oscillating in *dq* coordinates, was properly captured by the reduced model. As can be seen in Figs. 12 and 13, the microgrid safe region based on the switching system is Region I and Region II, gives a stable power range around 5.7 kW. Notice that the stable limit cycle curve gives the maximum and minimum peak values for the oscillations in the steady state.

The load parameter λ has a deep effect on the Hopf bifurcation (HB$_1$), as shown in Fig. 14. There is not a big difference between the washout and the cross virtual impedance in terms
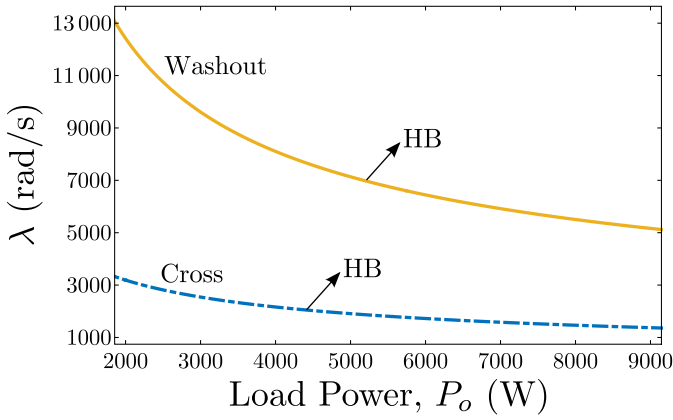
Fig. 14. Codimension-two bifurcation set showing the Hopf bifurcation (see HB$_1$ from Figs. 12 and 13), regarding P_o and λ as bifurcation parameters valid for both virtual impedance implementations.
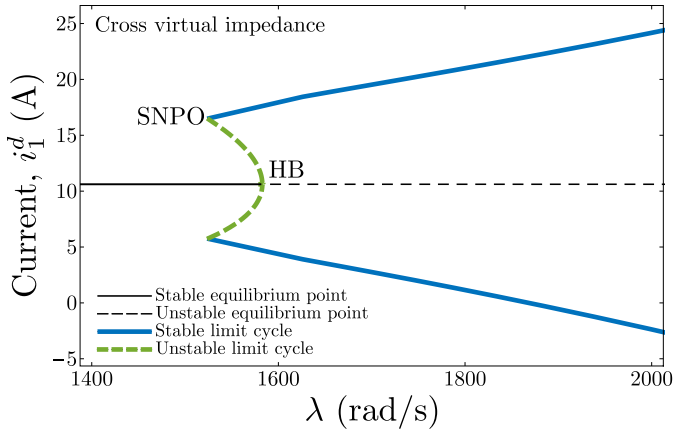

Fig. 16. Bifurcation diagram in the $\{\lambda, i_1^d\}$-plane for $P_o = 7$ kW, $X_v = 0.03\ \Omega$, and with the virtual impedance given by (5)-(6).

Fig. 15. Bifurcation diagram in the $\{\lambda, i_1^d\}$-plane for $P_o = 7$ kW, $X_v = 0.03\ \Omega$, and with the virtual impedance given by (3)-(4).

Fig. 17. Steps in the load power P_o and the effect on the active power from the first inverter for the cross virtual impedance implementation.

VII. SIMULATION RESULTS

The instabilities predicted by the reduced model can be validated by simulating the switching microgrid system (see Fig. 1) with the washout virtual impedance using the software PSIM. There are some small differences between the average models shown in Sections III and IV, and the simulations in this section. For instance, the ac-dc power converter control uses the measurement of the common bus voltages in the control laws, but in the simulation there is a low-pass filter with a cut-off frequency of 30 Hz. The presence of this filter increases the system stability, since the main source of problem is the interaction between the ac-dc power converters with the common bus voltage. Delays due to PWM and the discrete-time nature of controllers were accounted to the simulation, as they affect the system stability.

In order to illustrate the main operation regions of the microgrid depicted in Fig. 12, three steps in the load power P_o are applied as shown in Fig. 17. These load power steps were designed in such a way that when $t < 0.8$ s the system is operating in Region I with the load consuming $P_o = 1.25$ kW. In the interval 0.8 s $< t < 0.9$ s the system is in Region III ($P_o = 7.14$ kW) and for $t > 0.9$ s the microgrid is operating in Region IV ($P_o = 10$ kW). In Fig. 17, it can be observed that the average active power of the dc-ac power converter remains stable in the three operation regions. However, the currents i_1^d

of microgrid stability, but as Fig. 14 shows, for the occurrence of a Hopf bifurcation in the same power level, λ should be chosen different for each virtual impedance implementation as explained at the end of Section IV. It is possible to generate a bifurcation diagram for λ, for instance with P_o fixed at 7 kW as depicted in Fig. 15 for the cross virtual impedance, and in Fig. 16 for the washout version. Both bifurcation diagrams show the need for different λ values to each virtual impedance implementation.

Although the reduced model allows us to capture the main qualitative behavior of the microgrid dynamic, one of the drawbacks is the sensitivity of the Hopf bifurcation (HB$_1$) toward variations for the virtual impedance X_v. Any influence of X_v in the microgrid is not well captured by an instantaneous model for the VSI (Fig. 10 for the X_v effect on the full VSI model stability) and if there are instabilities due to source-source interaction, then a better source model must be used. One option to obtain better models is to use a similar approach to what was done to the ac-dc power converter reduced model, i.e., a first-order system applied to the instantaneous source equations. This procedure has the disadvantage of having to find the equivalent VSI time-constant.
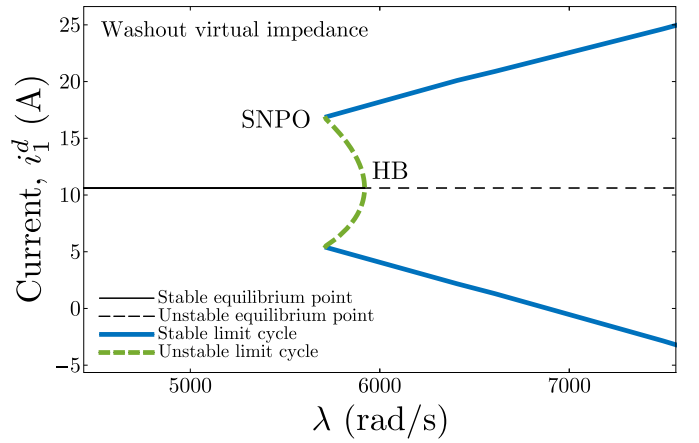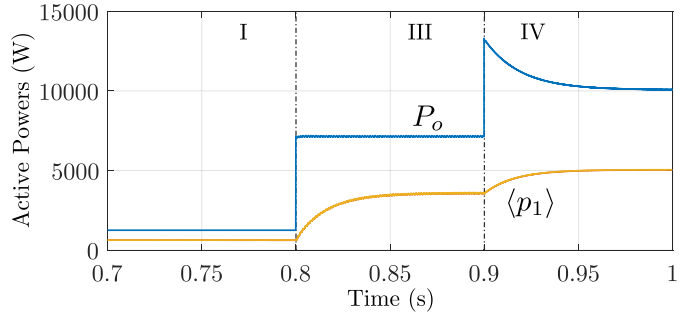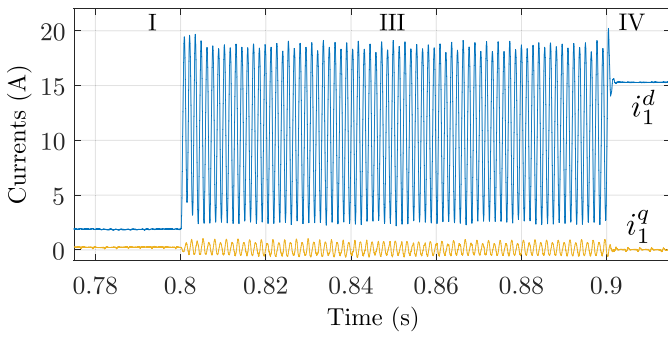
Fig. 18. Currents i_1^d and i_1^q for the operation Regions I, III, and IV.
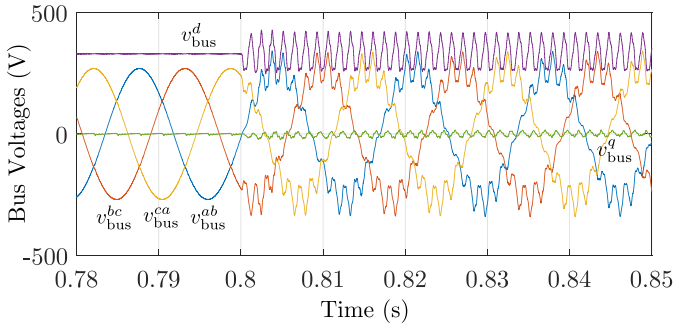

Fig. 19. Line-to-Line bus voltage in *abc* and *dq* coordinates when the Hopf bifurcation (HB$_1$) occurs at $t = 0.8$ s for a step in P_o from 1.25 kW to 7.14 kW is applied.
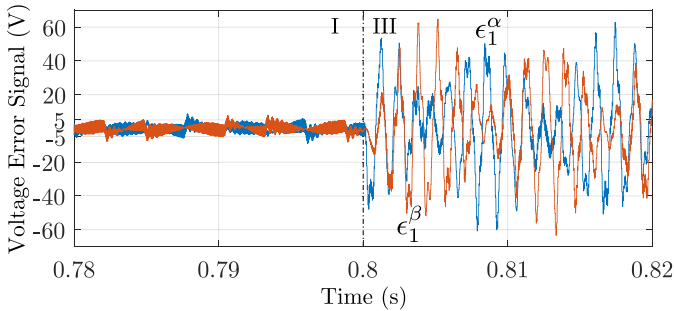

Fig. 20. Inverter voltage control loop error signals in $\alpha\beta$ when the Hopf bifurcation (HB$_1$) occurs at $t = 0.8$ s for a step in P_o from 1.25 kW to 7.14 kW is applied.

Fig. 21. AC-DC power converter load estimation when the Hopf bifurcation (HB$_1$) occurs at $t = 0.8$ s for a step in P_o from 1.25 kW to 7.14 kW is applied.

Fig. 22. AC-DC power converter output dc voltage for the operation Regions I, III, and IV.

Fig. 23. Current frequency spectrum for phase *a* only, $i_1^a + i_2^a$, when the Hopf bifurcation (HB$_1$) occurs.

and i_1^q are oscillating (stable limit cycle detected by bifurcation analysis, Fig. 12) in Region III, as shown in Fig. 18. The effect of the Hopf bifurcation (HB$_1$) can also be noticed on the bus voltage as shown in Fig. 19, on the VSI voltage error signals (56) as observed in Fig. 20, and in the ac-dc power converter, with the load estimation ($\hat{\mu}_1$) and the output dc voltage (v_1^{dc}) waveforms in Figs. 21 and 22, respectively.

Another consequence of the current oscillations generated by the Hopf bifurcation is the appearance of high frequency components, which increases the harmonic content in the inverter output currents and on the common bus voltage. Fig. 23 shows the phase *a* total source current ($i_1^a + i_2^a$) spectrum during the unstable regime, and it is possible to note that the Hopf bifurcation create new frequencies around 670 Hz a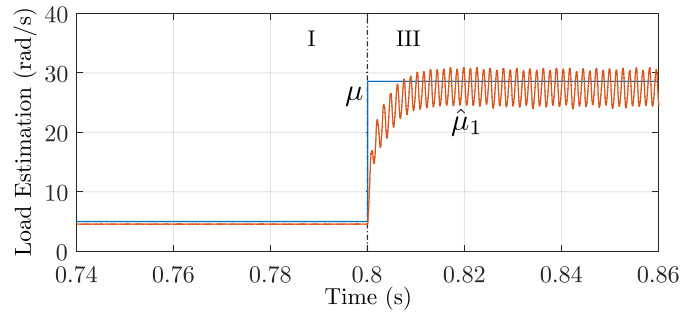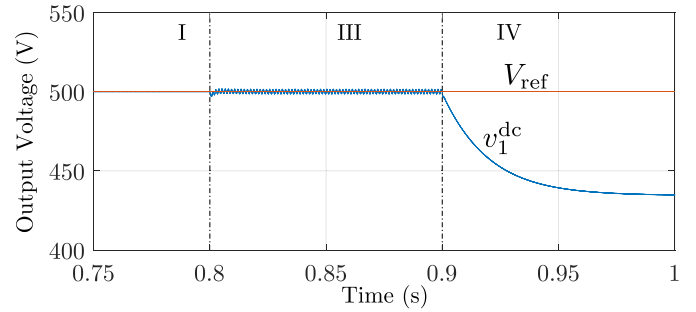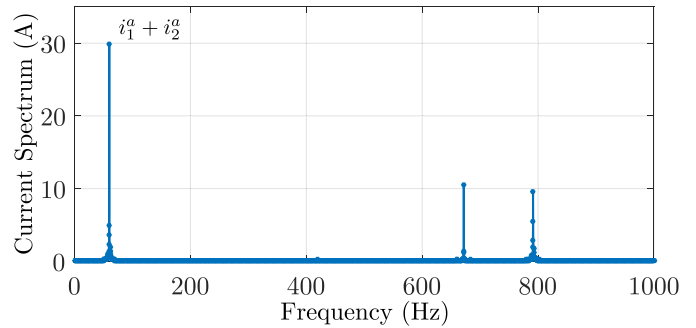nd 790 Hz. Although the output currents of both inverters oscillate, the low frequency active power exchanged between the inverters is small.

VIII. CONCLUSION

This paper has addressed the modeling and large signal stability analysis for a case study of an ac microgrid made of two parallel-connected inverters driving controlled ac-dc rectifier loads. The main dynamics phenomena that can occur when the power output varies have been analyzed through bifurcation analysis techniques applied to the reduced model of the system. This simplified case study is a first step to understand the dynamical behavior and the interaction between the different elements that exist in an ac microgrid.

Bifurcation diagrams obtained with the reduced model were validated by comparison with the simulation results obtained from the switching microgrid network (full microgrid system).

The reduced model and the techniques used to analyze the stability of the microgrid have proved to be useful for the microgrid design, despite the limitations regarding the virtual impedance. Furthermore, bifurcation diagrams have been demonstrated to be useful for selecting important parameters of the system, such as K_p, K_1, and K_2.

Acknowledgment

References

[1] J. C. Vasquez, J. M. Guerrero, M. Savaghebi, J. Eloy-Garcia, and R. Teodorescu, "Modeling, analysis, and design of stationary-reference-frame droop-controlled parallel three-phase voltage source inverters," *IEEE Trans. Ind. Electron.*, vol. 60, no. 4, pp. 1271–1280, Apr. 2013.

[2] E. C. Furtado, L. A. Aguirre, and L. A. B. Torres, "UPS parallel balanced operation without explicit estimation of reactive power—A simpler scheme," *IEEE Trans. Circuits Syst. II, Exp. Briefs*, vol. 55, no. 10, pp. 1061–1065, Oct. 2008.

[3] J. M. Guerrero, L. G. de Vicuna, J. Matas, M. Castilla, and J. Miret, "Output impedance design of parallel-connected ups inverters with wireless load-sharing control," *IEEE Trans. Ind. Electron.*, vol. 52, no. 4, pp. 1126–1135, Aug. 2005.

[4] V. Mariani, F. Vasca, J. C. Vasquez, and J. M. Guerrero, "Model order reductions for stability analysis of islanded microgrids with droop control," *IEEE Trans. Ind. Electron.*, vol. 62, no. 7, pp. 4344–4354, Jul. 2015.

[5] E. A. A. Coelho, P. C. Cortizo, and P. F. D. Garcia, "Small-signal stability for parallel-connected inverters in stand-alone ac supply systems," *IEEE Trans. Ind. Appl.*, vol. 38, no. 2, pp. 533–542, Mar./Apr. 2002.

[6] K. Yu, Q. Ai, S. Wang, J. Ni, and T. Lv, "Analysis and optimization of droop controller for microgrid system based on small-signal dynamic model," *IEEE Trans. Smart Grid*, vol. 7, no. 2, pp. 695–705, Mar. 2016.

[7] N. Bottrell, M. Prodanovic, and T. C. Green, "Dynamic stability of a microgrid with an active load," *IEEE Trans. Power Electron.*, vol. 28, no. 11, pp. 5107–5119, Nov. 2013.

[8] J. W. Simpson-Porco, F. Dörfler, and F. Bullo, "Synchronization and power sharing for droop-controlled inverters in islanded microgrids," *Automatica*, vol. 49, no. 9, pp. 2603–2611, 2013.

[9] J. Schiffer, R. Ortega, A. Astolfi, J. Raisch, and T. Sezi, "Conditions for stability of droop-controlled inverter-based microgrids," *Automatica*, vol. 50, no. 10, pp. 2457–2469, 2014.

[10] G. Diaz, C. Gonzalez-Moran, J. Gomez-Aleixandre, and A. Diez, "Scheduling of droop coefficients for frequency and voltage regulation in isolated microgrids," *IEEE Trans. Power Syst.*, vol. 25, no. 1, pp. 489–496, Feb. 2010.

[11] C. N. Onwuchekwa and A. Kwasinski, "Analysis of boundary control for buck converters with instantaneous constant-power loads," *IEEE Trans. Power Electron.*, vol. 25, no. 8, pp. 2018–2032, Aug. 2010.

[12] F. Zhang and Y. Yan, "Start-up process and step response of a Dc-Dc converter loaded by constant power loads," *IEEE Trans. Ind. Electron.*, vol. 58, no. 1, pp. 298–304, Jan. 2011.

[13] H. Akagi, Y. Kanazawa, and A. Nabae, "Instantaneous reactive power compensators comprising switching devices without energy storage components," *IEEE Trans. Ind. Appl.*, vol. IA-20, no. 3, pp. 625–630, May 1984.

[14] D. Marx, P. Magne, B. Nahid-Mobarakeh, S. Pierfederici, and B. Davat, "Large signal stability analysis tools in dc power systems with constant power loads and variable power loads—A review," *IEEE Trans. Power Electron.*, vol. 27, no. 4, pp. 1773–1787, Apr. 2012.

[15] E. Lenz, D. J. Pagano, and A. P. N. Tahim, "Codimension-two bifurcation analysis in DC microgrids under droop control," *Int. J. Bifurcation Chaos*, vol. 26, no. 2, 2016, Art. no. 1650028.

[16] J. He, Y. W. Li, and F. Blaabjerg, "An enhanced islanding microgrid reactive power, imbalance power, and harmonic power sharing scheme," *IEEE Trans. Power Electron.*, vol. 30, no. 6, pp. 3389–3401, Jun. 2015.

[17] J. He, Y. W. Li, J. M. Guerrero, F. Blaabjerg, and J. C. Vasquez, "An islanding microgrid power sharing approach using enhanced virtual impedance control scheme," *IEEE Trans. Power Electron.*, vol. 28, no. 11, pp. 5272–5282, Nov. 2013.

[18] M. Savaghebi, A. Jalilian, J. C. Vasquez, and J. M. Guerrero, "Secondary control scheme for voltage unbalance compensation in an islanded droop-controlled microgrid," *IEEE Trans. Smart Grid*, vol. 3, no. 2, pp. 797–807, Jun. 2012.

[19] H. Han *et al.*, "Review of power sharing control strategies for islanding operation of AC microgrids," *IEEE Trans. Smart Grid*, vol. 7, no. 1, pp. 200–215, Jan. 2016.

[20] T.-S. Lee, "Input-output linearization and zero-dynamics control of three-phase AC/DC voltage-source converters," *IEEE Trans. Power Electron.*, vol. 18, no. 1, pp. 11–22, Jan. 2003.

[21] A. Astolfi and R. Ortega, "Immersion and invariance: A new tool for stabilization and adaptive control of nonlinear systems," *IEEE Trans. Autom. Control*, vol. 48, no. 4, pp. 590–606, Apr. 2003.

[22] A. Dhooge, W. Govaerts, and Y. A. Kuznetsov. (2003). *Matcont: A MATLAB Package for Numerical Bifurcation Analysis of ODEs*. [Online]. Available: http://sourceforge.net/projects/matcont

[23] E. J. Doedel *et al.*, (1998). *Auto 97: Continuation and Bifurcation Software for Ordinary Differential Equations (With Homcont)*. [Online]. Available: http://indy.cs.concordia.ca/auto/

[24] B. Ermentrout, *Simulating, Analyzing, and Animating Dynamical Systems*. Philadelphia, PA, USA: SIAM, 2002.

[25] J. Guckenheimer and P. J. Holmes, *Nonlinear Oscillations, Dynamical Systems, and Bifurcations of Vector Fields*. New York, NY, USA: Springer, 1983.

Eduardo Lenz received the B.Sc. and M.Sc. degrees in electrical engineering from the Federal University of Ceará, Brazil, and the Ph.D. degree in control and automation engineering from the Federal University of Santa Catarina, Brazil. His main research interests are nonlinear control applied to power electronics, adaptive control, nonlinear dynamics, bifurcation analysis, hamiltonian system, and electromagnetic fields.

Daniel J. Pagano was born in La Plata, Argentine, in 1961. He received the B.Sc. degree in telecommunications engineering from the National University of La Plata, Argentine, in 1985, the M.Sc. degree in electrical engineering from the Federal University of Santa Catarina, Brazil, in 1989, and the Ph.D. degree in robotics, automation and electronics from the University of Seville, Spain, in 1999. He is currently a Professor with the Department of Automation and Systems, Federal University of Santa Catarina. From 2006 to 2007, he was a Visiting Professor with the Department of Engineering Mathematics, University of Bristol, U.K. He was a Visiting Professor with the Australian Energy Research Institute, University of New South Wales, Sydney, for 11 months, in 2016. His main research interests include nonlinear dynamical systems, bifurcation analysis, nonlinear control, and power electronics.

Josep Pou (S'97–M'03–SM'13–F'17) received the B.S., M.S., and Ph.D. degrees in electrical engineering from the Technical University of Catalonia (UPC), Catalonia, Spain, in 1989, 1996, and 2002, respectively.

In 1990, he joined the Faculty of UPC as an Assistant Professor, where he became an Associate Professor in 1993. From 2013 to 2016, he was a Professor with the University of New South Wales (UNSW), Sydney, Australia. He is currently an Associate Professor with the Nanyang Technological University, Singapore. From 2001 to 2002 and from 2005 to 2006, he was a Researcher with the Center for Power Electronics Systems, Virginia Tech, Blacksburg. From 2012 to 2013, he was a Visiting Professor with the Australian Energy Research Institute, UNSW. Since 2006, he has been collaborated with Tecnalia Research & Innovation as a Research Consultant. He has authored over 230 published technical papers and has been involved in several industrial projects and educational programs in the fields of power electronics and systems. His research interests include modulation and control of power converters, multilevel converters, renewable energy, energy storage, power quality, HVDC transmission systems, and more-electrical aircraft and vessels.